PUBLICATIONS OF THE ASTRONOMICAL SOCIETY OF THE PACIFIC, **111**:238–245, 1999 February

A NICMOS3 Camera for Fringe Detection at the IOTA Interferometer

R. MILLAN-GABET AND F. P. SCHLOERB

Physics and Astronomy Department, University of Massachusetts at Amherst, Amherst, MA 01003; rmillang@comet.phast.umass.edu, schloerb@comet.phast.umass.edu

AND

W. A. TRAUB AND N. P. CARLETON

Harvard-Smithsonian Center for Astrophysics, 60 Garden Street, Cambridge, MA 02138; traub@cfa.harvard.edu, ncarleton@cfa.harvard.edu

Received 1998 September 16; accepted 1998 November 2

ABSTRACT. We describe a new instrument, based on a NICMOS3 array, for the detection of interference fringes in the near-infrared at the Infrared-Optical Telescope Array. The camera saw "first fringes" in Spring of 1997 and has since been in routine use for a variety of astrophysical investigations. We present its design characteristics and parameters, which result in magnitude limits for fringe detection of $J = 8.4$, $H = 8.5$, and $K' = 6.5$.

1. INTRODUCTION

The Infrared-Optical Telescope Array is a collaborative project between Harvard University, the Smithsonian Astrophysical Observatory, and the University of Massachusetts at Amherst to develop a Michelson stellar interferometer for optical and infrared (IR) wavelengths (Traub 1998). It is located at SAO's F. L. Whipple Observatory on Mount Hopkins, Arizona.

As of this writing, the IOTA consists of two 0.45 m telescopes locatable at 17 stations along an L-shaped track with arms of 15 and 35 m and south/east and north/west orientations, respectively. Installation of a third telescope began in the Summer of 1998. The maximum baseline at IOTA is $B = 38$ m, which corresponds to an angular resolution of $\sim\lambda/B = 7$, 9, and 12 mas in the J, H, and K bands, respectively.

In order for interference to be detected in the presence of atmospheric turbulence, the telescopes must sample a portion of the incoming wavefront over which the phase variations are small (typically 50 cm in the near-IR). Moreover, the detection of the interferogram must be made in a time shorter than the time scale for atmospheric phase fluctuations (typically 50 ms in the near-IR). These requirements severely limit the number of photons available, and place a high premium on detector efficiency.

The original IR instrumentation of the IOTA, which was derived from the earlier IRMA interferometer (Dyck, Benson, & Ridgway 1993), consisted of a pair of discrete InSb photovoltaic detectors. This system had a limiting magnitude for interferometric observations of about 2 in the K band and was successful in achieving the initial milestones and scientific results (Dyck et al. 1995). However, there was a clear need for a more sensitive detection system that would enable observations of fainter sources and study of a wider range of interesting astrophysical problems.

NICMOS3 arrays (developed by Rockwell International Science Center) are increasingly becoming the detector of choice as IR imagers due to their low noise, large format, high quantum efficiency (QE), low dark current and high uniformity. Although in this application we do not make use of the imaging capabilities of the NICMOS3 (only two pixels are needed), it proved to be the best choice for being at the heart of our new camera. This conclusion was reached after comparison with other IR detectors available to us, and based on a calculation in which a linear least squares fit to a model of the interferometer's response is used to estimate the signal-to-noise ratio (SNR) of fringe parameters (Millan-Gabet et al. 1995[1]).

In addition to the electronics upgrade, the IR optics have also been upgraded for this instrument in order to replace the previous set of undersized and somewhat damaged optics. The resulting increase in flux and decrease in wavefront degradation has further improved our sensitivity for the detection of interference fringes.

2. THE UMASS/SAO NICMOS3 CAMERA

The NICMOS3 focal plane array (Kozlowski et al. 1993; Cooper et al. 1993) consists of 256 × 256 HgCdTe integrating detectors organized in four independent 128 × 128 quadrants. The pixel size is 40 μm. The quantum efficiency (QE) of the detectors is better than 50% for wavelengths in the range 0.9–2.5 μm.

[1] Millan-Gabet, R., Schloerb, F. P. Traub, W. A., & Dyck, H. M. 1995, IOTA Technical Report, available on the world wide web at http://donald.phast.umass.edu/~rmillang/rmg_pubs.htm

In brief, the operation of a NICMOS3 array is as follows: The pixels in the array are selected for readout via a *X*-*Y* addressing scheme that is controlled by one horizontal and one vertical shift register (H-SR and V-SR, respectively). The pixel (x, y) of a given quadrant is addressed by sequentially clocking a *high* state into position x of the H-SR and into position y of the V-SR, starting at pixel (1,1), which is located by convention at the upper left corner of each quadrant, facing the illuminated side of the detector. In principle, these two steps can be done in any order, or even simultaneously, although we found that the array's output amplifier exhibits less severe transients when clocking vertically first to reach the target row and then horizontally to reach the target pixel. At any time during this sequence it is possible to *clear* both SRs in order to start a new readout cycle.

The accumulated charge in the pixel that is being addressed is reproduced on a sampling capacitor (one per pixel) and sensed by the output amplifier (one per quadrant), which provides a voltage signal that is approximately linearly related to the accumulated number of electrons in the pixel well at the time of sampling. The time derivative of this voltage is approximately equal to the incident photon rate times a constant gain factor. At the output of the NICMOS3, this signal has approximately 0.5 volt of full dynamic range and an offset of about 3 volts under typical operating conditions, although both of these values depend on how exactly the array is biased. A pixel is saturated after it has integrated about 300,000 electrons, discharging the sampling capacitor, which must then be *reset* by addressing the pixel and enabling the reset clock. This restores the voltage to its initial value with an uncertainty of order 100 electrons. However, in the usual mode of operation the array (or pixel of interest) is reset and then read out at least once before and after the integration period, the signal of interest being the difference between the two reads, which subtracts out this initial uncertainty.

The dominant source of noise in integrating arrays is read noise, the uncertainty associated with determining the charge accumulated by a pixel. In this respect, a key characteristic of the architecture of the NICMOS3 array is that a pixel that is being addressed can be sampled multiple times nondestructively and without changing the charge on the pixel, at least in principle. To the extent that the read noise is purely random, N such multiple reads may be averaged in order to reduce the read noise by $\sqrt{N}$. We will show an experimental test of this supposition in § 3.2 below.

2.1. Optics

At the IOTA, star light leaves the individual telescope assemblies, which include a star tracker for correction of wavefront tip-tilt errors, in afocal beams and travel inside evacuated pipes towards the laboratory located at the corner of the array. In order to achieve optical path equalization as the star undergoes its sidereal motion, the light from one of the telescopes is sent to a delay line, a section of which consists of a dihedral mirror mounted on an air-bearing track capable of precise and smooth motion under interferometric control. The beams then exit the vacuum enclosure and travel in air inside the laboratory to the optical tables.

The setup for beam combination and detection on the IR optical table is shown schematically in Figure 1. Dichroic mirrors separate the visible light, which is used by the star tracker servo system, from the science IR light. Interference is achieved by combining the beams from the two telescopes in the pupil plane, at a beam splitter, resulting in two complementary outputs (π radians out of phase). The two combined beams are then focused onto two pixels of the NICMOS3 array by an f/6 parabola and a small f/1 lens (not shown) placed 1.9 mm in front of the detector surface. With this arrangement, approximately up to 60% of the starlight reaching the detector can be focused on each of the two target pixels.

An interference fringe is recorded as a mirror (M1) mounted on a piezo stack (Coldwell, Papaliolios, & Traub 1998) scans a 30 μm stroke around the zero OPD position at a rate of up to 10 scans per second. The precise frequency of this scanning mirror is chosen as a compromise between sensitivity (more integration time per sample for lower scanning frequencies) and piston error (interferogram phase fluctuations during the measurement). This system allows a large number of fringe packets to be recorded per observation (typically 500) in only a few minutes, which provides a substantial sample on which to perform a statistical estimation of fringe visibility in the presence of wavefront errors induced by the turbulent atmosphere.

The optical axis intersects pixel (32,32) of the selected quadrant, and the two target pixels can be placed about 10 pixels apart on the same row, ensuring quick access. In our current application, we use quadrant 3 of the detector, giving negligible contamination of the signal by the glow from the quadrant's output amplifier, which is located at the opposite corner. Optical baffling in the Dewar allows these target positions to vary by about ± 2 pixels in x or y without noticeable loss of light. Figure 2 is a photograph of the lower section of the Dewar assembly.

2.2. Camera Readout

2.2.1. Readout Electronics

As described above, the detector requires a set of analog bias levels in order to power the chip and set its dynamic range, as well as a set of digital clocks required to read out the array and trigger the ADC conversions. A block diagram of the control electronics for the camera is shown in Figure 3.

A card box is located immediately behind the Dewar that contains the bias card responsible for generating six precise, low noise bias levels. This box also contains a card for conditioning the digital signals going to the detector and the ADC

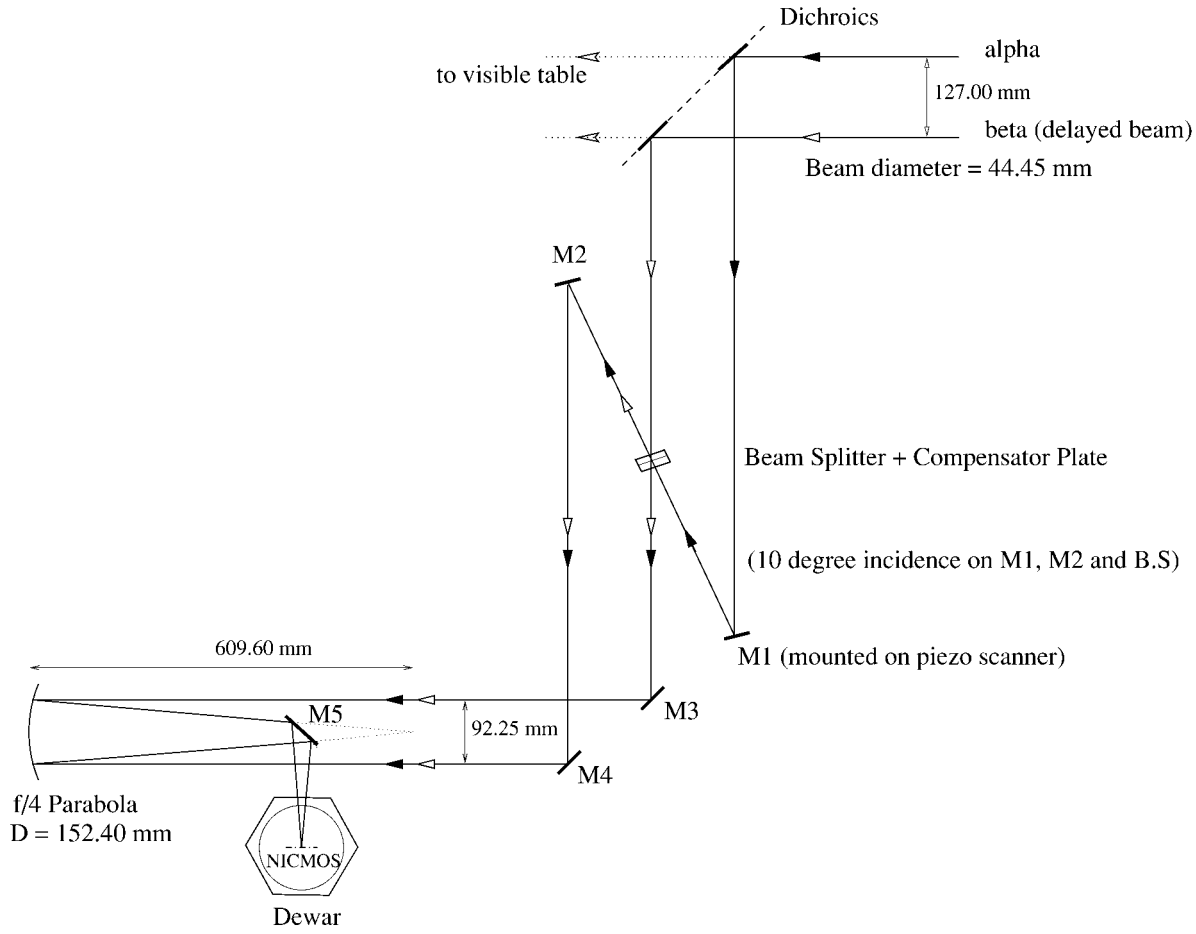

FIG. 1.—IR table optical layout

card, and connects to the in-Dewar electronics through about 0.3 m of individually shielded twisted-pair cables.

The digital waveforms required to address the pixels, clear the SRs, reset the pixels, and trigger the A/D conversions originate in a Pentium PC via programmed I/O. This method allows clocking through the pixels (for fast access to the target pixels) at a rate of up to 400 KHz. We clock the four quadrants in parallel, but connect the output of only one of them to the rest of the signal chain.

In order to minimize stray electrical pickup, a low-noise dc amplifier is placed inside the Dewar, at approximately room temperature. The amplifier has a gain of about 20 and an adjustable bias, which serves to cancel the dc offset present in the raw signal. Its output leaves the Dewar and connects to the ADC card along a path that is physically well separated from the bias and clocking wires. The A/D converter has 16 bits of resolution over its 10 volt input range, and a conversion time of 10 μs, which includes 2 μs required by the sample and hold circuitry. To the total conversion time we add 11 μs for the detector output to settle after a pixel has been addressed.

All of the digital signals as well as the data returned by the A/D converter are opto-isolated from the PC environment. All the cards are custom made, four layer printed circuit boards with separate analog and digital sections and two layers dedicated to power and ground planes.

2.2.2. Readout Software

The readout of the NICMOS3 array is controlled by programmed I/O from a dedicated Pentium PC running a C++ program under DOS. This program executes its data acquisition sequence in response to *start*, *stop* commands sent by a Macintosh Quadra computer, which is also responsible for controlling the sidereal position of the delay line, real time data display, and data storage. The acquisition of the fringes is synchronized with the sweep of the piezo scanner: at the start of its travel, the piezo sends a TTL signal that triggers a *reset* of the NICMOS3 pixels and marks the start of a new scan containing an interferogram. A block diagram showing this system hierarchy is shown in Figure 4.

During the scan, 256 data points are collected as the NICMOS3 pixels accumulate photons and discharge. Each of those

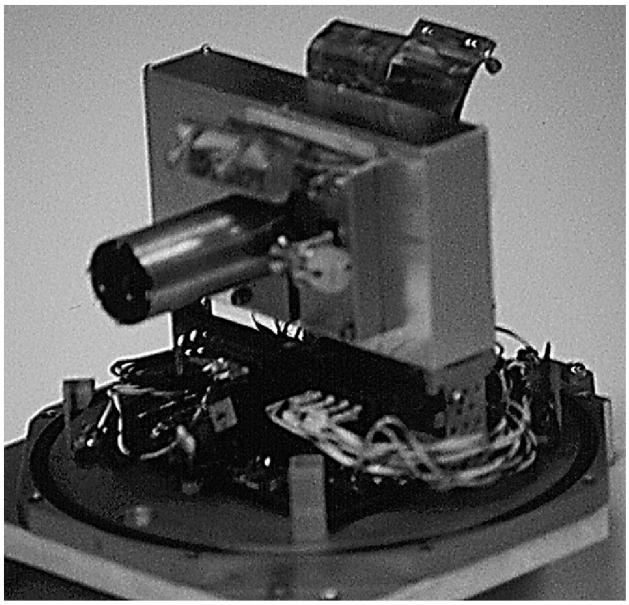

FIG. 2.—Photograph of the bottom section of the Dewar assembly, showing part of the radiation shield enclosing (following the direction of a light beam): a beam stop, optical baffle, filter wheel box and detector card box. Also visible are the cooling copper straps as well as part of the amplifier electronics (located under the cold shield).

data points corresponds to the following readout frame being executed by the Pentium:

1. Loop N1 times:
2. Clock to target row.
3. Clock to 1st target column.
4. Sample pixel 1 N2 times.
5. Clock to 2nd target column.
6. Sample pixel 2 N2 times.
7. Calculate average of $N_{\rm reads} = N1 \cdot N2$ reads and subtract from previous value.

The minimum frame time that we can achieve with this method is 0.18 ms, corresponding to sampling each pixel once ($N1 = N2 = 1$). In general the frame time is $t(\text{frame}) = N_1(a + 2bN_2)$, where $a \simeq 120$ μs and $b \simeq 21$ μs. We note that the frame time is divided between the outer (N1) and inner (N2) loops in order to minimize the difference between the instants at which the fringes in pixels 1 and 2 are sampled.

2.3. Cooling

The Dewar is a standard He cooling design, adapted for our needs, in which both cryogenic cans are filled with LN_2. The inner can provides direct cooling to the detector and optical baffles and has a hold time of over 24 hours. The outer can cools the radiation shield and has a hold time of less than 12 hours.

Thermal coupling between the LN_2 reservoir and the back of the NICMOS3 chip is via thin flexible copper straps that cool the detector to about 80 K with a $1/e$ time of approximately 1 hour. A Lake Shore temperature sensor and a resistor are mounted close to the chip for sensing and possible heating. For temperatures in the range 80–100 K the dark current from the device is expected to be 0.2–100 electrons s^{-1} (Cooper et al. 1993) and is therefore completely negligible for the 1 ms integration times characteristic of our readout modes. Temperature control in this range could be desirable because the QE is expected to improve at higher temperatures, particularly at the shorter J and H wavelengths (Rieke et al. 1993). However, this behavior was not confirmed in a test in which we varied the temperature of the detector between 77 and 180 K while recording the signal obtained from background illumination through the K' filter. We found the signal to be constant to within $\pm 0.9\%$ throughout this range. We terminated this test at 180 K because the scattered light glow from the resistor heater began to illuminate the detector.

The detector is physically located on a printed circuit board placed inside a cooled light-tight box (see Fig. 2), which is in turn inside the radiation shield. Electrical connections between the detector and the warm electronics are via 0.005 inch diameter copper-constantan wires in order to minimize heat transfer. Attached to the front of this box is the filter wheel assembly that carries three standard J, H, and K' filters, a set of H and K' plus a 5% ND filter and an opaque stop. The filter wheel is rotated manually via a mechanical feed-through in the Dewar wall.

3. SENSITIVITY, NOISE, AND MAGNITUDE LIMITS

3.1. Sensitivity

We measure the sensitivity S of the system by observing stars of known magnitude m, for a time interval t (ms) and fitting the results to an equation of the form

$$S(\text{electrons}) = S_0 t 10^{(-0.4 \cdot m)}, \text{ or } \mathrm{S(adu)} = S(\text{electrons})/g, \quad (1)$$

where $g = 3.2$ electrons/adu is the gain (see § 3.2 below). We find

$$S_0(J) = 10{,}938 \text{ electrons ms}^{-1},$$

$$S_0(H) = 11{,}824 \text{ electrons ms}^{-1},$$

$$S_0(K') = 10{,}524 \text{ electrons ms}^{-1},$$

At K' there is an additional background signal $B = B_0 t$, where $B_0 = 586$ electrons ms^{-1}.

These measurements also allow us to trivially calculate the optical efficiency (OE) of the IOTA in the near-IR by comparing the above values with the expected photon rate collected by our apertures from a 0th magnitude star. Assuming a nominal

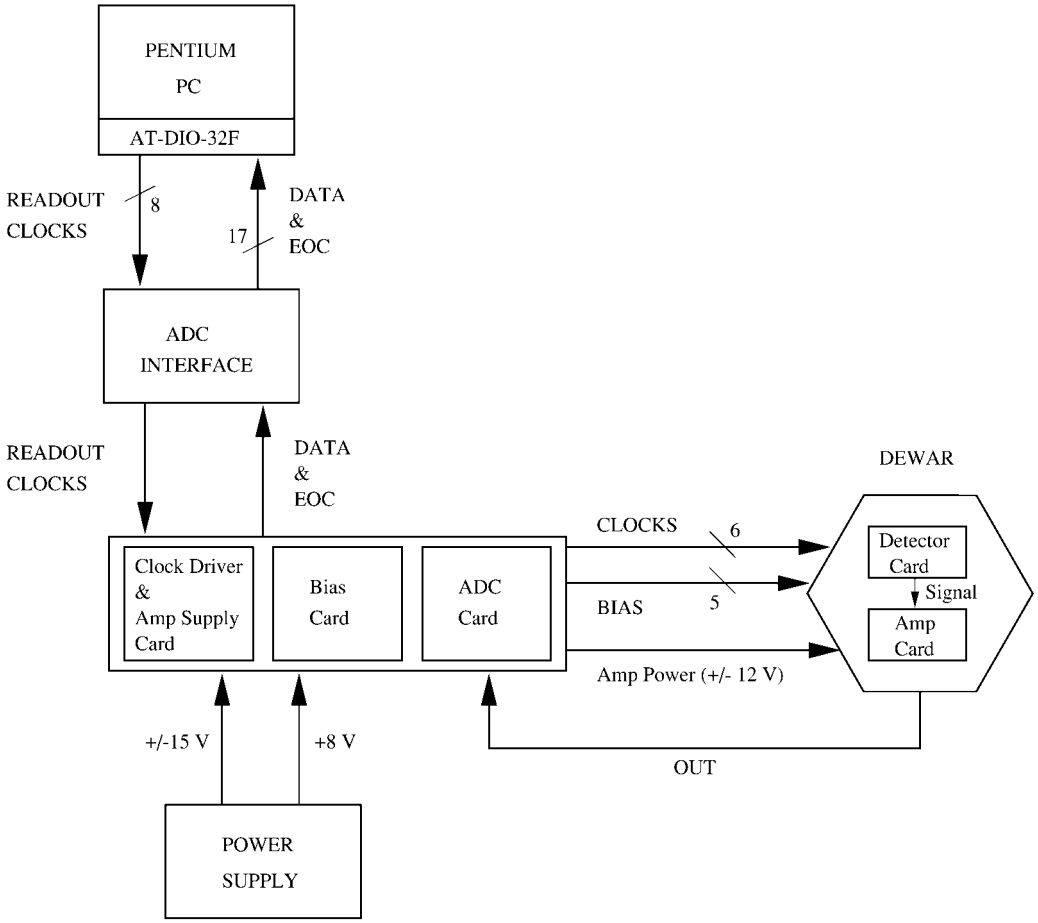

FIG. 3.—Block diagram showing the camera control electronics

value of 60% for the detector QE, we obtain for our three spectral bands: OE(J) = 2.1%, OE(H) = 4.5% and OE(K') = 7.7%. These OE factors include the propagation of the light through the interferometer and beam combination table, as well as the efficiency in focusing each light beam splitter output onto a single NICMOS3 pixel.

3.2. Read Noise

In order to determine the read noise for this camera experimentally, we performed the standard experiment of recording the mean and variance measured for various light levels on the detector. Under Poisson statistics, the slope of the σ^2(mean) curve gives the gain in adu/electron and the read noise ($\sigma_{\rm read}$) is given by extrapolating to the variance obtained with no light incident on the detector. In this experiment the light flux was changed using a variable dc light source; a pixel was accessed and the corresponding signal was measured from the difference between reads before and after a constant integration time of about 10 ms. Figure 5 shows the results obtained, from which we calculate the following: gain = 3.2 electrons/adu and $\sigma_{\rm read}$ = 16.6 electrons for double reads. The measured gain agrees very well with the design value. Note that for a single read the read noise should be $\sqrt{2}$ smaller, or about 12 electrons.

The effect on the read noise of averaging multiple samples was measured by recording scans, using the readout mode described in § 2.2.2 above, with no light incident on the detector (looking at the sky through the J filter). The rms of the 256 points in each scan was calculated for scans recorded under various readout modes, corresponding to N = 1, 4, 8, 12, 16, and 40 multiple reads per sample. The median in each scan was also calculated, in order to subtract the shot noise associated with the increasing dark current from the total scan rms: σ_N(adu) = [(scan_rms)^2 − median/gain]$^{1/2}$. The results are shown in Figure 6, where it can be clearly seen that multiple sampling greatly reduces the read noise. In the ideal case (*dashed curve*) the read noise would decrease as $\sqrt{N}$ for arbitrarily large numbers of reads. In practice, however, the data are best fitted (*solid line*) with an additional constant source of noise ($\sigma_{\rm min}$ = 3.7 electrons); so that the improvement is not as rapid as in the ideal case beyond about 10 reads, and saturates

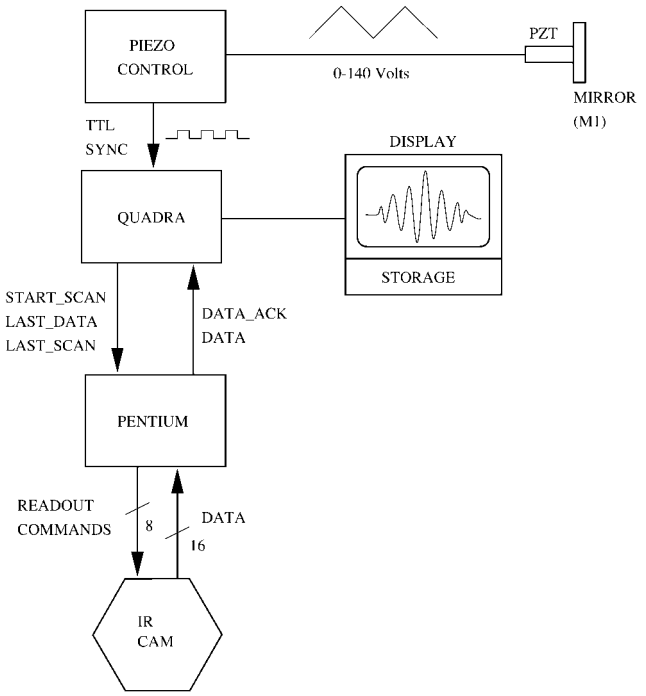

FIG. 4.—Block diagram showing the data acquisition control

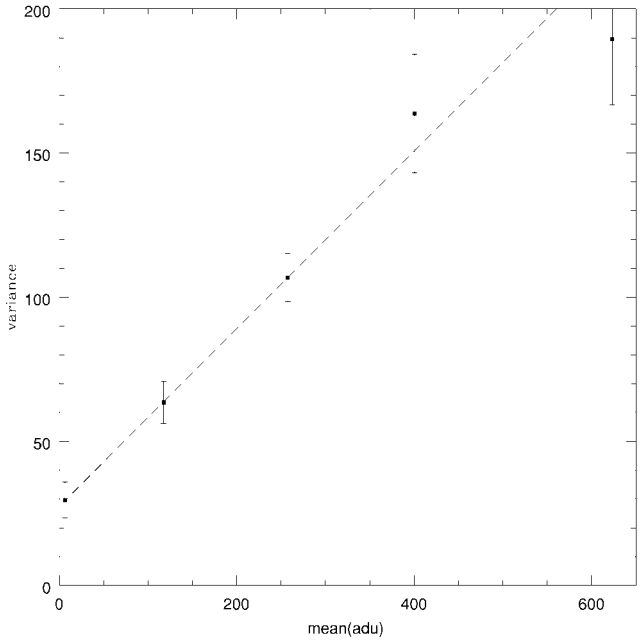

FIG. 5.—Variance curve, from which we measure the system parameters: gain = 3.2 electrons/adu and read noise = 16.6 electrons/double read.

beyond about 200 reads. Specifically, we use the relations

$$\sigma^2_{\text{total}} = \sigma^2_N + \sigma^2_{\text{ph}}, \tag{2}$$

$$\sigma^2_N = (\sigma^2_{\text{read}} + \sigma^2_{\text{min}})g^{-2}, \tag{3}$$

$$\sigma^2_{\text{ph}} = [S(\text{electrons}) + B(\text{electrons})]g^{-2}. \tag{4}$$

We note, however, that in our slowest practical readout mode (see § 3.3 below) we have time to sample each pixel about 32 times, which is still well within the regime in which significant noise reduction is achieved by multiple sampling.

The value of the read noise could also be calculated from Figure 6 by using the $N = 1$ case. The value thus obtained is $\sigma_1 = 24.6$ electrons, or 32% different from the value obtained with the variance curve experiment (16.6 electrons). We believe that this discrepancy arises from the fact that the array readout modes were very different: in the second experiment each data point in the scan involves connecting and disconnecting the pixel from the sampling circuitry, perhaps introducing additional noise. Since this is also the readout mode used during for fringe detection, in the calculations that follow we use the larger noise estimate.

3.3. Magnitude Limits for Fringe Detection

This new instrument has been in routine operation at the IOTA since 1997 September. As an illustration, Figure 7 shows an H band interferogram measured on the star HD 65666, of magnitude $H = 6.9$. The figure shows the filtered difference of the two complementary interferograms, and the SNR in the central fringe is about 7.

In the absence of absolute metrology to ensure that the zero OPD point is inside the 60 μm OPD window that is scanned, each interferogram must be detected with sufficient SNR in real time, and this constraint sets the magnitude limit that we can achieve (although once a fringe has been detected, it is in

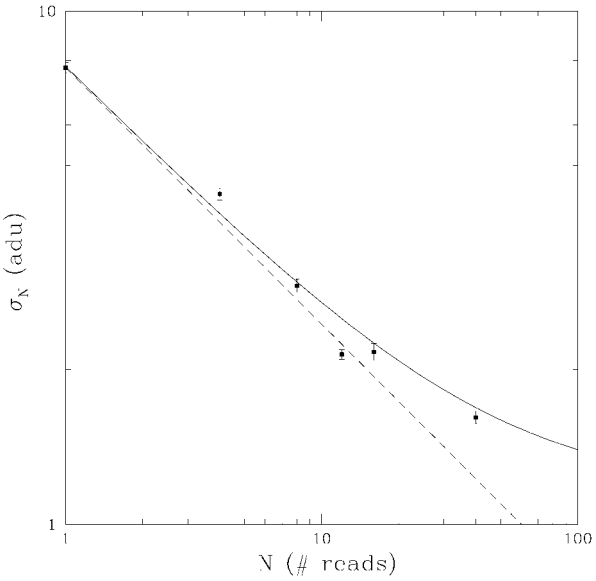

FIG. 6.—Reduction of read noise by multiple sampling. The dashed line corresponds to the ideal slope of −1/2.

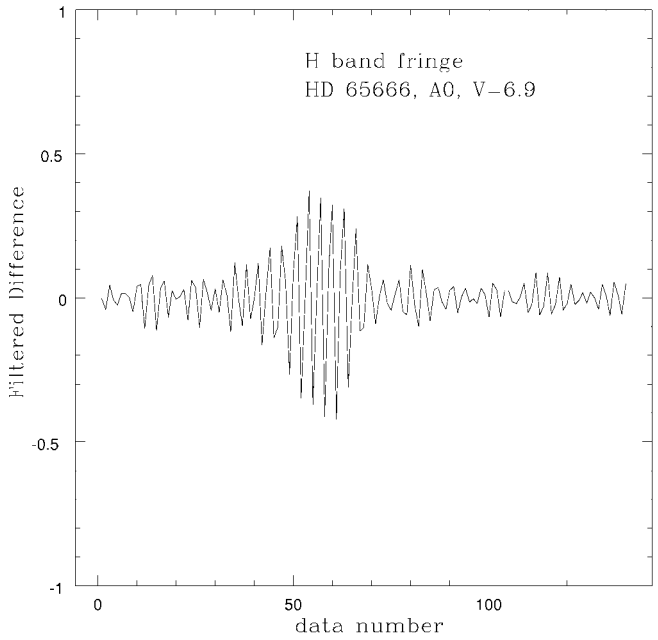

FIG. 7.—Interferogram (difference between the two outputs divided by the sum, bandpass filtered) measured on the star HD 65666 ($H = 6.9$).

principle possible to improve the accuracy of the fringe parameters measured by co-adding many fringes).

The basic observable in a two-telescope interferometer is the contrast of the fringes, or fringe visibility V. If I denotes the signal detected in one of the pixels, this quantity is defined as $V = (I_{\max} - I_{\min}) / (I_{\max} + I_{\min})$ and is related by a Fourier Transform to the brightness distribution of the source being observed (see e.g. Goodman 1985). We evaluate the fringe detection limits by calculating the SNR in the measurement of the fringe visibility from a single interferogram. The following expression is obtained by least squares fitting of the interferometer's response (see footnote 1)

$$\mathrm{SNR}_V = \sqrt{2}\sqrt{\frac{0.48\sqrt{2\pi}}{4}}\sqrt{M}V_oV_i\mathrm{SNR}_{\mathrm{Ph}}. \qquad (5)$$

In the above equation, the $\sqrt{2}$ factor arises from the subtraction of the complementary beam splitter outputs, the second numerical factor is a consequence of assuming a Gaussian spectral shape and M is the number of samples within the $1/e$ full width of the Gaussian envelope (about seven fringes at K'). The fringe visibility can be written as the product of object visibility (V_o) and an instrumental factor (V_i), which represents the degradation in fringe contrast by the turbulent atmosphere and imperfections in the optics and alignment of the interferometer. The photometric SNR in each interferogram sample is given by

$$\mathrm{SNR}_{\mathrm{Ph}} = \frac{S}{\sigma_{\mathrm{total}}}. \qquad (6)$$

TABLE 1
LIMITING MAGNITUDES FOR FRINGE DETECTION

Band	NICMOS3	Photon Limit
J	8.4	9.9
H	8.5	10.9
K'	6.5	6.5

Magnitude limits for fringe detection are derived using equations (1) and (2) and the following operational parameters. The slowest fringe frequency that can be tolerated in the presence of atmospheric piston errors is about 100 Hz, and if each fringe is sampled 5 times, then the maximum sampling time per data point is $t = 2$ ms. During this time we can perform $N = 32$ multiple reads. For observations of an unresolved object ($V_o = 1.0$) and considering a typical value for the instrumental plus atmospheric visibility of $V_i = 0.5$, we obtain the magnitude limits listed in Table 1. The photon limited case, $\sigma_{read} = 0$, has been included for comparison. We note that in the K' band we are limited by background, which results in the lower sensitivity. The values in Table 1 are independently validated by estimating the SNR in interferograms of the faintest sources we have observed, under less favorable conditions: HR 65666 ($J = 6.9$, $H = 6.9$) and HR 2991 ($K' = 6.2$).

4. FUTURE IMPROVEMENTS

Work is currently under way in order to achieve even better sensitivity with this system. The in-Dewar optics and baffling design are being modified in order to achieve the best possible focus on the target pixels while reducing the background at K', thus improving the sensitivity in this band. For reference, the above calculation gives $m_K(\mathrm{Limit}) = 8.4$ if we assume zero background. Also, the detector card is being modified in order to accommodate a PICNIC array, Rockwell's upgrade device for the NICMOS3, which is expected to result in lower readout noise.

Finally, the overall design of this PICNIC camera is being duplicated for use as an IR star tracker. This will again enable new science to be done at the IOTA by allowing observations of sources that do not have enough visible flux to be tracked by the CCD star trackers.

We are indebted to a number of people for making significant contributions to this instrument. Ta-Chun Li was responsible for the design of the readout electronics. John Karakla, Barry Stone, John Geary, and Paul Horowitz provided crucial advice on electronics. Charlie Hughes machined the Dewar components and optical mounts. Charles Coldwell assisted in inter-

facing the camera to the interferometer's main control software. Marc Lacasse assisted with on-site operations. We thank Kadri Vural, Robert Bailey, Scott Cabelli, and Craig Cabelli at Rockwell International Science Center for their courtesies to us and guidance in using the NICMOS3 detector. We also acknowledge financial support from NSF grant number AST 9528129 as well as from the University of Massachusetts and the Smithsonian Astrophysical Observatory.

REFERENCES

Coldwell, C. M., Papaliolios, C. D., & Traub, W. A. 1998, Proc. SPIE 3350, Astronomical Interferometry, 424
Cooper, D. E., et al. 1993, Proc. SPIE 1946, Infrared Detectors and Instrumentation, 170
Dyck, H. M., Benson, J. A., & Ridgway, S. T. 1993, PASP, 105, 610
Dyck, H. M., et al. 1995, AJ, 109, 378
Goodman, J. W. 1985, Statistical Optics (New York: Wiley-Interscience)
Kozlowski, L. J., et al. 1993, Proc. SPIE 1946, Infrared Detectors and Instrumentation, 148
Rieke, M. J., et al. 1993, Proc. SPIE 1946, Infrared Detectors and Instrumentation, 214
Traub, W. A. 1998, Proc. SPIE 3350, Astonomical Interferometry, 848